1   Changes in global teleconnection patterns under global warming and stratospheric aerosol

2   intervention scenarios

3   **Abolfazl Rezaei[1, 2, *], Khalil Karami[3], Simone Tilmes[4], & John C. Moore[5, 6, 7]**

4

5   [1] Department of Earth Sciences, Institute for Advanced Studies in Basic Sciences, Zanjan 45137–

6   66731, Iran. arezaei@iasbs.ac.ir; abolfazlrezaei64@gmail.com.

7   [2] Center for Research in Climate Change and Global Warming (CRCC), Institute for Advanced Studies

8   in Basic Sciences (IASBS), Zanjan 45137–66731, Iran.

9   [3] Institut für Meteorologie, Stephanstraße 3, 04103 Leipzig, Germany. khalil.karami@uni-leipzig.de

10   [4] National Center for Atmospheric Research, Boulder, CO, USA. tilmes@ucar.edu

11   [5] College of Global Change and Earth System Science, Beijing Normal University, Beijing, 100875,

12   China. john.moore.bnu@gmail.com

13   [6] CAS Center for Excellence in Tibetan Plateau Earth Sciences, Beijing, 100101, China.

14   [7] Arctic Centre, University of Lapland, Rovaniemi, 96101, Finland.

15

16   * Corresponding Author: Abolfazl Rezaei, Department of Earth Sciences, Institute for Advanced

17   Studies   in   Basic   Sciences,   Zanjan   45137–66731,   Iran.   arezaei@iasbs.ac.ir;

18   abolfazlrezaei64@gmail.com.

19

20

21   **Abstract**

22   We investigate the potential impact of Stratospheric Aerosol Intervention (SAI) on the

23   spatiotemporal behavior of large-scale climate teleconnection patterns represented by the North

24   Atlantic Oscillation (NAO), Pacific Decadal Oscillation (PDO), El Niño/Southern Oscillation (ENSO)

25   and Atlantic Multidecadal Oscillation (AMO) indices using simulations from the Community Earth

26   System Models (CESM1 and CESM2). The leading Empirical Orthogonal Function of sea surface

27   temperature (SST) anomalies indicates that greenhouse gas (GHG) forcing is accompanied by

28   increases in variance across both the North Atlantic (i.e., AMO) and North Pacific (i.e., PDO) and a

29   decrease over the tropical Pacific (i.e., ENSO); however, SAI effectively reverses these global

30   warming-imposed changes. The projected spatial patterns of SST anomaly related to ENSO show no

31   significant change under either global warming or SAI. In contrast, the spatial anomaly patterns

32   pertaining to AMO (i.e., in the North Atlantic) and PDO (i.e., in the North Pacific) changes under global

33   warming are effectively suppressed by SAI. For AMO, the low contrast between the cold-tongue

34   pattern and its surroundings in the North Atlantic, predicted under global warming, is restored under

35   SAI scenarios to similar patterns as in the historical period. The frequencies of El Niño and La Niña

36   episodes modestly increase with GHG emissions in CESM2, while SAI tends to compensate for them.

37   All climate indices' dominant modes of inter-annual variability are projected to be preserved in both

38   warming and SAI scenarios. However, the dominant decadal and interdecadal variability mode

39   changes induced by global warming are exacerbated by SAI, particularly in the Atlantic-based AMO.

40   Nonetheless, these findings are limited by the data available, especially for multi-decadal signals,

41   with less than 100-year long simulations available for SAI.

42   **Keywords:** Ocean-atmosphere teleconnection patterns; GLENS; SSP5-8.5; Stratospheric Aerosol

43   Intervention; Global warming

44

45   **500-character non-technical text**

46   Teleconnection patterns are important characteristics of the climate system, well-known examples

47   include the El Niño and La Niña events driven from the tropical Pacific. We examined how patterns

48   that arise in the Pacific and Atlantic Oceans behave under stratospheric aerosol geoengineering and

49   greenhouse gas (GHG)-induced warming. In general, geoengineering reverses trends, however in the

50   Atlantic, the multidecadal oscillation that is shifted to higher frequencies by GHG is further

51   strengthened.

52

53   **1. Introduction**

54   Although the Paris agreement and accompanying international commitments to decrease carbon

55   emissions are an essential step forward, current nationally contributions have only about a 50%

56   chance to restrict global mean temperature increase to 2°C above preindustrial (Meinshausen et al.,

57   2022). Exceeding 2°C will lead to severe consequences and societal disruption worldwide as

58   humanity is critically dependent on ecosystems, food, fresh water, and health systems which face

59   rapidly challenging adaptation pressure above 2°C of global warming (Field and Barros, 2014).

60   In parallel with emissions reductions, solar radiation modification (SRM) has been suggested to limit

61   global temperature increases and consequent climate impacts from anthropogenic greenhouse gas

62   (GHG) emissions. A naturally occurring analog of SRM is the well-known global surface cooling

63   following large volcanic eruptions, albeit over relatively short periods. Simulations have shown that

64   SRM decreasing total solar irradiance by about 2%, would roughly compensate for global warming

65   from a doubling of CO_2 concentrations (Dagon and Schrag, 2016).

Oceans act as major drivers of climate variability worldwide (e.g., Shukla, 1998; Cai et al., 2021), and more than 90% of the excess energy balance of the earth arising from GHG emissions ends up heating the ocean (Cheng et al., 2015). Variations in sea surface temperatures (SSTs) and the global climate are linked through ocean-atmosphere energy exchanges that can be helpfully summarized by climate indices that characterize large-scale climate teleconnection patterns. That is recurring and persistent, large-scale anomaly patterns of pressure and circulation across large geographical regions. Some of the most referred to are El Niño/Southern Oscillation (ENSO), Pacific Decadal Oscillation (PDO), Atlantic Multidecadal Oscillation (AMO), and North Atlantic Oscillation (NAO). The dominant inter-annual feature of climate variability on the planet is ENSO, and its state produces widespread climatic and environmental outcomes (Latif and Keenlyside, 2009). The PDO modulates marine ecosystems and global climate on decadal time scales (Mantua et al., 1997), impacts ENSO onset and frequency (Fang et al., 2014), and is useful for short- to long-term climate forecast (An and Wang, 1999). The AMO has broader hemispheric impacts beyond North American and European climates (Enfield et al. 2001), influencing the monsoons across North African, East Asia, and India (Zhang and Delworth 2006). The NAO is among the dominant climate variability modes in the northern hemisphere (Simpkins, 2021).

Several studies have explored how climate indices, particularly ENSO, respond to global warming and increasing GHG concentrations. Statistically significant systemic changes have occurred in ENSO dynamics and the evolution of El Niño and La Niña events since the 1960s (Moron et al., 1998; Capotondi and Sardeshmukh, 2017). ENSO may favor more severe events under global warming (Fedorov and Philander, 2001), and Cai et al. (2015) found that ENSO-associated disastrous weather consequences tend to arise more frequently under unabated CO_2 emissions. Cai et al. (2021) found an inter-model consensus on increases in forthcoming ENSO rainfall and temperature fluctuations under increasing GHG concentrations. The PDO, which is essentially the extra-tropical manifestation of ENSO, is simulated with a similar spatial pattern as at present under various future climates but with reduced amplitude and a shorter characteristic time scale (e.g., Zhang and Delworth, 2016). The North Atlantic is a key ocean for investigating global climate changes (Wang and Dong, 2010), and acts as a major carbon dioxide sink (Watson et al., 2009). Atmospheric CO_2 concentrations vary with the phase of the AMO with the warm phase associated with lowered atmospheric CO_2 (Wang and Dong, 2010). The two NAO action points in the Icelandic low and the Azores high have been projected to significantly intensify and shift northeastward by 10-to-20° in latitude and 30-to-40° in longitude in response to global warming (Hu and Wu, 2004).

98   Stratospheric Aerosol Intervention (SAI), is a type of SRM that has been widely simulated by many

99   global climate models (e.g., Kravitz et al., 2013), which is accompanied by changing in global

100 circulations such as the NAO teleconnection pattern (Moore et al., 2014), and is known in various

101 models to partially offset the decline in the Atlantic Meridional Overturning Circulation (AMOC; Xie

102 et al., 2022). Undorf et al. (2018) simulated the North Atlantic SST cooling accompanied by the

103 historical rise of stratospheric sulfate aerosol from North America and Europe dating back to 1850-

104 1975. Gabriel and Robock (2015) is the only study to date that explores the effects of SAI in multiple

105 models on the possible amplitude and frequency changes of El Niño/Southern Oscillation (ENSO).

106 They concluded that changes in ENSO in the SAI simulations were either not present or not large

107 enough to be captured by their approach, given the across-model variability issue. Thus, little is

108 known about possible changes that future global climate change scenarios with artificial cooling may

109 have on ocean-atmosphere climate indices. Recently, a novel set of SRM models have been globally

110 complete with the state-of-the-art climate models: Community Earth System Model versions 1 and

111 2 (CESM1 and CESM2). These models have improved planetary boundary layer turbulence, aerosols,

112 radiation, and cloud microphysics which should enable more reliable for the forthcoming global

113 climate change projections (Mills et al., 2017).

114 We use the Geoengineering Large Ensemble Simulation (GLENS) with 20 members from a single

115 model, the Community Earth System Model 1 (CESM1) with Stratospheric Aerosol Intervention

116 (GLENS-SAI), to explore the possible changes in climate teleconnection patterns under future climate

117 change scenarios. The models use the Representative Concentration Pathway (RCP) 8.5 high GHG

118 emissions forcing state (Riahi et al., 2011) as a baseline and increase stratospheric sulfur injections

119 through the century, to maintain global surface temperatures at 2020 levels. This produces an

120 increasingly large signal-to-noise ratio through the 21st century. In addition, we use recent

121 simulations (SSP5-8.5-SAI) with an updated model version (CESM2). For these simulations, the SSP5-

122 8.5 GHG emissions scenarios were used as the GHG baseline on which SAI was performed. The two

123 different model experiments show some surprising differences in the required sulfur injections and

124 climate outcomes with and without SAI applications (Fasullo et al., 2020, Tilmes et al., 2020). Thus,

125 even models from different generations in the same family can produce sufficiently different climates

126 to explore a range of plausibly real climate impacts. The goal of this study is to identify robust features

127 across the two model versions in the response of climate indices (ENSO, PDO, AMO and NAO) to GHG

128 induced global warming and its compensation by SAI.

129 We employed empirical orthogonal functions and wavelet transforms to decompose time series and

130 study the differences in the climate teleconnection patterns between the SSP5-8.5 and SSP5-8.5-SAI

131 scenarios. Since teleconnection patterns are emergent features of the non-linear, chaotic climate

132 system (Ghil et al., 2002), their underlying physical causes are complex and not necessarily the same

133 in any model as on the real planet. Hence, we assess the potential changes in temporal and spatial

134 characteristics of climate indices of AMO, NAO, ENSO, and PDO under both extreme warming GHG

135 scenarios and with SAI employed to mitigate those warmings while maintaining extreme GHG

136 concentration trajectories.

137

138 **2. Data and Methods**

139 **2.1. Models and scenarios**

140 We used two SAI models and scenarios: (1) CESM1 for GLENS-SAI and (2) CESM2 for SSP5-8.5-SAI.

141 The GLENS simulations were done by the Community Earth System Model version 1 (CESM1) with

142 the Whole Atmosphere Community Climate Model (WACCM) as the atmospheric system integrated

143 to land, ocean, and sea ice models (Mills et al., 2017). The resolution of atmospheric component is

144 1.25° in longitude and 0.9° in latitude. A 20-member reference simulation for the RCP8.5 scenario

145 (Riahi et al., 2011) over the 2010–2030 period with three ensemble members (001 to 003)

146 continuing up to the end of the 21st century. GLENS-SAI is a 20-member ensemble of stratospheric

147 sulfur dioxide (SO_2) injection simulations, spanning 2020-2099. Each ensemble member was begun

148 in 2010 with small differences in their initial air temperatures, while their ocean, sea-ice, and land

149 temperatures were the same. Even before the start of the SAI injections in 2020, the fully coupled

150 model produced variability between the ensemble members due to its chaotic nature. Here, we use

151 all available members of the RCP8.5 and GLENS-SAI simulations, which extend until the end of the

152 21st century. For the analysis, we used monthly SST and sea-level pressure (PSL).

153 We also analyzed output from the NCAR Community Earth System Model version 2- Whole

154 Atmosphere Community Climate Model Version 6 (CESM2(WACCM6)). This model version was used

155 for performing the Coupled Model Intercomparison Project Phase 6 (CMIP6; Eyring et al., 2016)

156 simulations. Like GLENS, this SAI experiment is according to the high GHG emissions scenario, called

157 SSP5-85 in CMIP6, (SSP5-8.5-SAI) and limits mean global temperatures to 1.5°C above 1850–1900

158 conditions, which without SAI, is exceeded around the year 2020 in CESM2(WACCM6) under SSP5-

159 8.5. The experiment used sulfur injection locations at the same four latitudes as in GLENS to

160 accomplish the same three temperature goals (Tilmes et al., 2020). We used the monthly SST and PSL

161 data from all five members (r1 to r5) of the SSP5-8.5 scenario (covering 2015-2100) and the three

162 available ensemble members of SSP5-8.5-SAI that cover the period of 2020-2100. For the analysis,

163 we also applied a one-member historical simulation based on the specific CESM1(WACCM) version

164   used for GLENS between 1980-2009 (denoted as "historical" in the following). All three

165   corresponding members (r1 to r3) from the CESM2(WACCM6) version were used for the historical

166   period.

167   The SAI scenarios using both CESM1 and CESM2 inject SO_2 at four predefined points (30°N, 30°S,

168   15°N, and 15°S) at ~5 km above the tropopause using a feedback controller to maintain not just the

169   global mean temperature, but the interhemispheric and equator-to-pole temperature gradients.

170   Fasullo and Richter (2022) explain the inter-model differences in the aerosol mass latitudinal

171   distributions between the SAI experiments using CESM1 and CESM2. CESM2 SAI utilizes the CMIP6

172   SSP5-8.5 experiment as a baseline which has been used by various modeling teams (Tilmes et al.,

173   2020) while CESM1 SAI uses the well-known RCP8.5 scenario. In GLENS-SAI, most of the aerosols

174   were injected at 30°N and 30°S with much smaller injection mass at 15°N and a tiny amount at 15°S

175   while for SSP5-8.5-SAI, the highest concentrations were released at 15°S, modest mass at 15°N and

176   30°S, and a small amount at 30°N. These differences in the SO_2 distributions across the two SAI

177   scenarios for CESM1 and CESM2 produce a range of variability in shortwave radiation and cloud

178   responses to CO_2 concentration increases (Fasullo and Richter, 2022). Additionally, Fasullo and

179   Richter (2022) identified that changes in the spatial salinity and density patterns in the Atlantic

180   Ocean, and in turn, the Atlantic Meridional Overturning Circulation (AMOC), are very different under

181   GLENS-SAI compared to SSP5-8.5-SAI experiment. These differences between SAI simulations

182   represent part of the system variability.

183   The equilibrium climate sensitivity (ECS) of CESM2-WACCM is 4.75 °C and lies in an ECS range of 1.83

184   to 5.67 °C from 41 different CMIP6 GCMs (IPCC AR6, 2021). The absolute mean surface temperature

185   difference between CESM2-WACCM and historical records (0.89 °C) and is also within the range of

186   0.38-1.23 °C from 37 different CMIP6 models (Scafetta, 2021). CESM2 is one of the best nine models

187   for simulating precipitation worldwide when measured by the Hellinger distance between bivariate

188   empirical densities of 34 CMIP6 models and the historical data from Global Precipitation Climatology

189   Centre (GPCC; Abdelmoaty et al., 2021). Additionally, the global-mean values of SST, summer land

190   temperatures, precipitation, and ECS simulated by CESM1 and CESM2 are roughly similar to each

191   other as well as compatible with the historical values over the 1985-2014 period (Danabasoglu et al.,

192   2020; Table S1).

193   Relative to the preindustrial 1851-1850 period, CESM2-WACCM projects global mean surface air

194   temperature rises of ~6.25 °C by the 2071-2100 period under SSP5-8.5 which compares with the

195   range of ~3.3-6.6 °C from 35 ensembles of 12 CMIP6 models (Cook et al., 2020).

196

2.2. Climate indices

The AMO was calculated from the area-weighted average of SSTs across the northern Atlantic from 0-70° N. The NAO was computed from the PSL time series at two stations: Gibraltar (to the south of Spain; around 36.1°N and 5.3°W) and Reykjavik (in the southwest of Iceland; around 64.1°N and 22.0°W). The ENSO index follows the definition proposed by Trenberth (1997). Here, we used SSTs at the Niño 3.4 region (east-central equatorial Pacific between 5°N-5°S, 170°W-120°W) as a proxy for ENSO. After removing the global mean SST anomaly, the leading Empirical Orthogonal Function (EOF) of monthly SST anomalies across the North Pacific (20°–70°N) is termed PDO following Mantua et al. (1997). All these computations were analyzed through the Climate Data Toolbox prepared by Greene et al. (2019). As an example, Fig. 1 compares AMO, NAO, ENSO, and PDO indices obtained from SSP5-8.5 and SSP5-8.5-SAI scenarios.

We characterized ENSO by El Niño and La Niña episodes. The ENSO index positive and negative episodes correspond to El Niño and La Niña, respectively. Consistent with Gabriel and Robock (2015), ENSO episodes were identified as departures of at least 0.5 standard deviations from zero in a five-month running averaged ENSO time series. Each episode was characterized by its duration (years), the extreme peak excursion (°C), and the width at half extreme height (years).
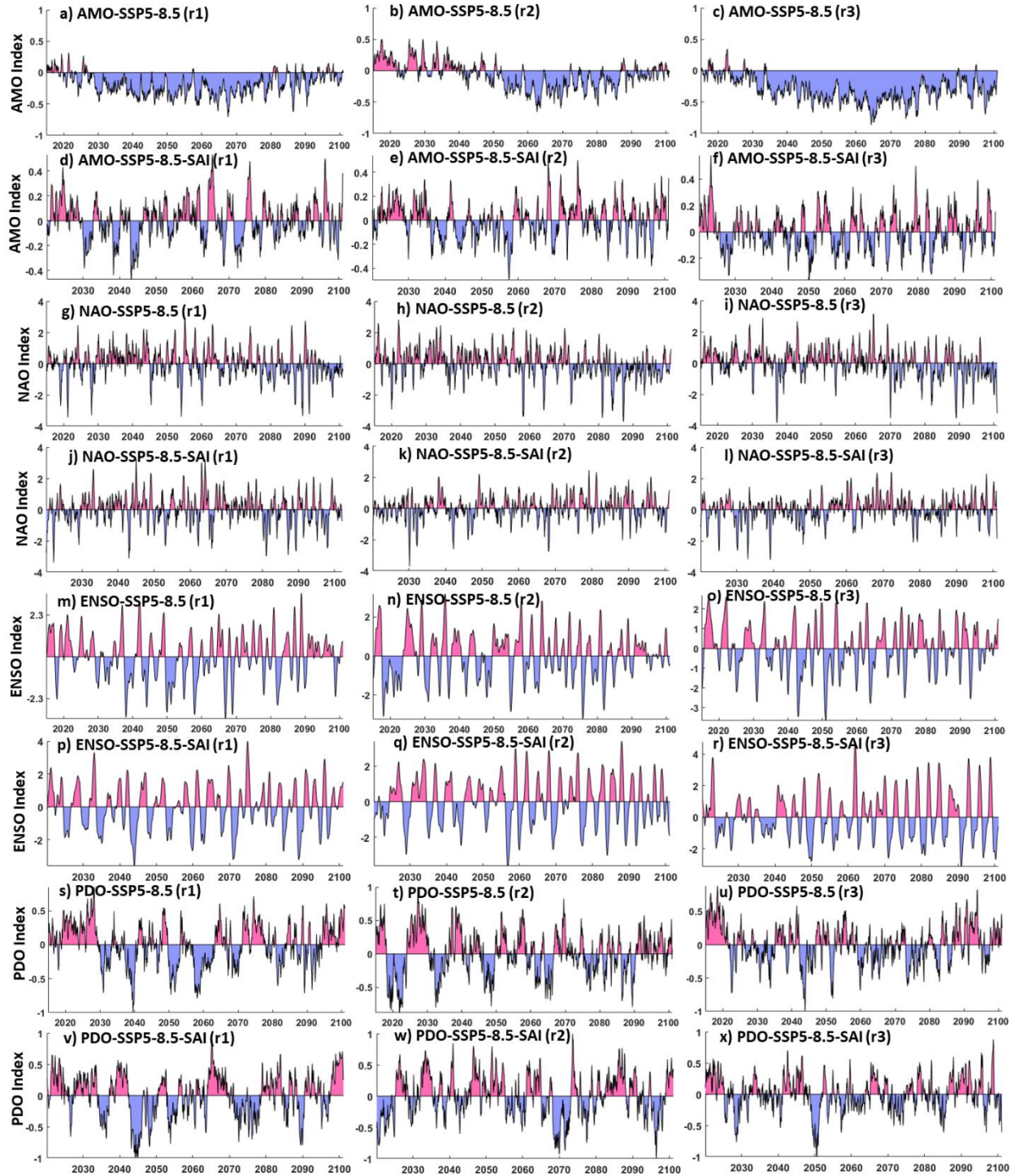
Figure 1. AMO (panels a-f), NAO (panels g-l), ENSO (i.e., NINO3.4, panels m-r), and PDO (panels s-x) indices obtained from ensemble members r1(left column), r2 (middle column), and r3 (right column) of the SSP5-8.5 (odd rows) and SSP5-8.5-SAI (even rows) scenarios.

2.3. Spatiotemporal analyses

Analyses in both space and time as well as modes of variability ranging from the inter-annual through decadal, to inter-decadal changes were used to identify the possible changes in the large-scale climate circulations resulting from global warming and SAI scenarios. EOF analysis is commonly used to extract the climate variability space-time modes (e.g., Chen and Tung, 2018; Joyce, 2002). We applied EOF to extract the first (dominant) modes of de-trended non-seasonal-SST and its corresponding variance across the North Atlantic and North Pacific, which are related to the AMO and PDO respectively. As ENSO is the primary indicator of global climate variability, we used the leading EOF of global SST anomalies in the study of ENSO.

The continuous wavelet transform (CWT) is commonly used to capture the primary characteristics of signals (Addison, 2018). For a time series (x_n, n=1, . . . , N) having regular time intervals δt, the CWT is computed as the convolution of x_n with the scaled and normalized wavelet (e.g., here we use the Morlet wavelet which gives reasonably equal weighting and resolution in time and period space; Grinsted et al., 2004):

$$W_n^X(s) = \sqrt{\frac{\delta t}{s}} \sum_{n'=1}^{N} x_{n'} \psi_0 \left[(n'-n)\frac{\delta t}{s} \right] \text{ where } \psi_0(\eta) = \pi^{-1/4} e^{i\omega_0 \eta} e^{-0.5\eta^2} \tag{1}$$

where s is the wavelet scale, ψ_0 the Morlet wavelet, ω_0 dimensionless frequency, [*] the complex conjugate, and η dimensionless time. The noise spectrum assigned to generate significance testing is a key issue in time series analysis. We concurred with the widely-used red-noise null hypothesis methodology based on 1000 synthetic series with the same mean, standard deviation and first-order autoregressive coefficient as the target time series produced by Monte Carlo approaches to estimate the significance of the CWT (Grinsted et al., 2004). Additionally, for each time series, CWT's global power spectrum was calculated as a function of time. The global power spectrum provides insight into the dominant temporal modes of variability of each climate index within each ensemble member for the reference GHG and SAI scenarios. The wavelet method cone of influence automatically shows where the periods analyzed are being influenced by the end of the time series. Thus, the longest periods can only be reliably assessed for the middle of the time series.

The individual ensemble members are treated as independent of each other in calculating the statistics of the ensembles. The CWT was conducted on monthly ENSO time series, and the 12-month moving averaged low-pass filtered signals of AMO, NAO, and PDO. We always use the longest available record length in every ensemble member to gain maximum statistical power to establish significant differences between experiments.

3. Results:

3.1. Changes in the spatial patterns

Figure 2 reveals the projected changes in the variance of the SST anomalies related to the AMO (i.e., across the North Atlantic), ENSO (i.e., global scale), and PDO (i.e., across the North Pacific) based on CESM1 and CESM2 results. Figure S1 shows three different plots for the CESM1 as the time period of the 20-member ensemble for RCP8.5 differ: ensembles 001 to 003 (2010-2097) are longer than the other 17 ensemble members (2010-2030). For RCP8.5 and SSP5-85 using CESM1 and CESM2, respectively, the strong GHG forcing and global warming to the end of the 21st century increases the variance of the first EOF SST anomaly in the North Atlantic and North Pacific (representing AMO and PDO), but reduces the variance of the leading EOF in global SST anomaly (related to ENSO). Based on the statistical t-test results, the changes in the means imposed by global warming relative to historical are all significant except one case (Fig. 2f). Differences between SAI and historic in CESM2 values of the leading EOF variance of AMO and ENSO are not significant, showing that the significant changes under GHG forcing are effectively reversed by SAI. In contrast, the changes in PDO variance imposed by global warming using CESM1 relative to historical remain significant under SAI. Using CESM2, there is no significant changes in the PDO variance from historical to global warming, or to SAI.
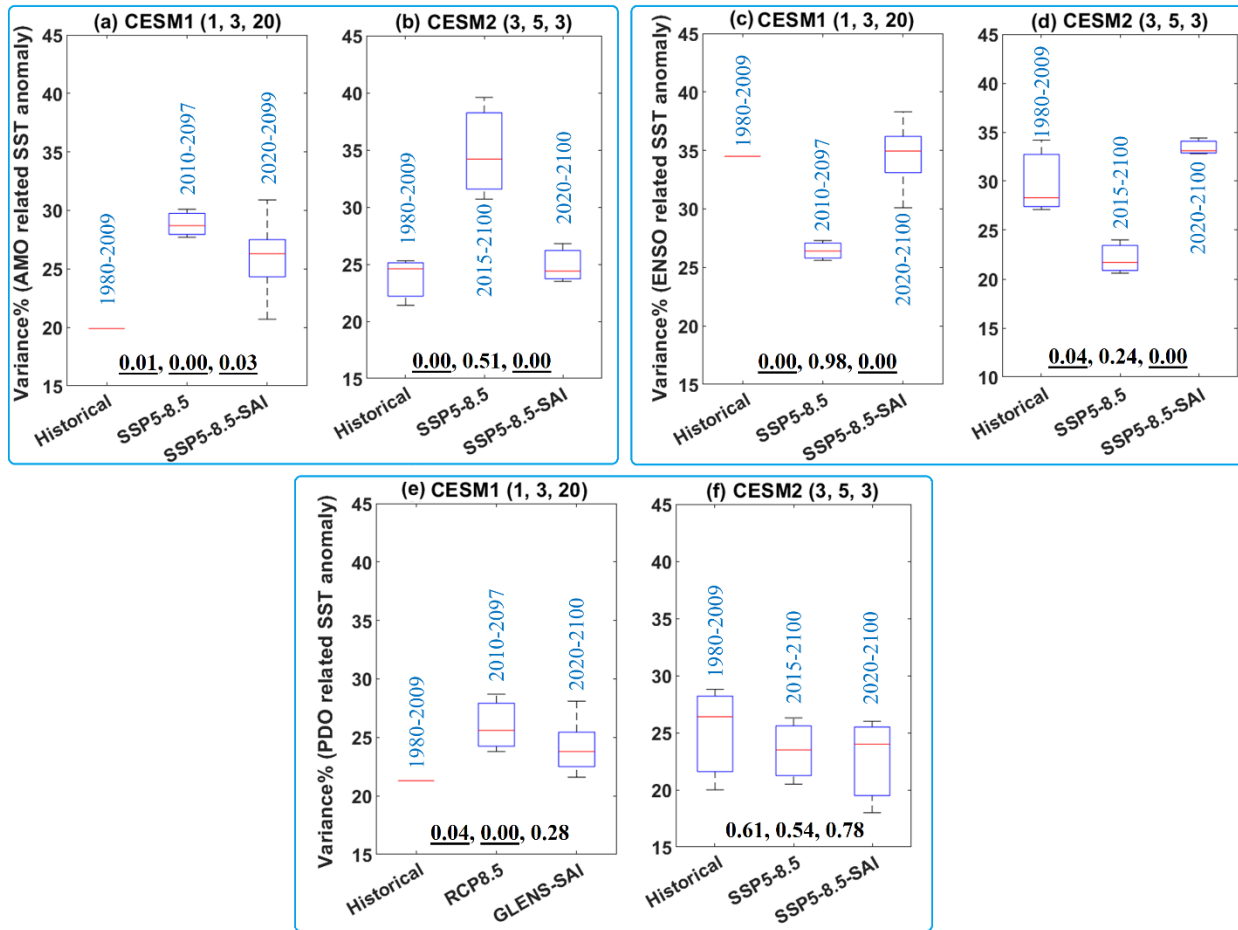
**Figure 2.** Box and whiskers plot of the variance in the leading EOFs, representing AMO, PDO, and ENSO, relative to the total variance of the SST fields: AMO across the North Atlantic (top-left panel); ENSO (top-right panel) global SST; and PDO across the North Pacific (bottom panel). The values in blue on each column box show the period of the data for historical, GHG (i.e., RCP-8.5 and SSP5-8.5), and climate intervention (GLENS-SAI and SSP5-8.5-SAI) scenarios. The titles of each subplot refer to the CESM version and the number of ensembles used in the historical, GHG (RCP8.5 and SSP5-8.5), and SAI (GLENS-SAI or SSP5-8.5-SAI) scenarios, respectively. The median for each experiment is denoted by the red line, the upper (75th) and lower (25th) quartiles by the top and bottom of the box and ensemble limits by the whisker extents. The three values shown at bottom of each sub-plot refer to the p-values obtained from the statistical t-test between historical and global warming, historical and SAI, and global warming and SAI, respectively. Values underlined are significant (i.e., $p<0.05$)

Figures 3-6 and S2-S3 show the spatial anomalies of the leading EOF mode of the SST in the North Atlantic, North Pacific, and tropical pacific under both the CESM1 and CESM2. For the historical period, there is a cold-tongue pattern in the North Pacific broadens from the western to the eastern parts surrounded by warm water, particularly to the north. GHG related global warming lowers the contrast between the cold-tongue pattern and its surroundings and increases the water temperature inside the cold-tongue-pattern, and also leads to a substantial expansion of a warm-pattern in the

288   north. The same patterns (Fig. 4) are also obtained under SSP5-8.5 using CESM2. SAI effectively
289   shrinks the warm pattern in the northern Atlantic under the RCP8.5 and SSP5-8.5 through a
290   significant SST decrease, particularly using CESM1 (bottom row in Figs. 3 and 4). The SSP5-8.5-SAI
291   experiment increases the temperature contrast in the cold-tongue pattern, while the GLESN-SAI does
292   not. The projected changes in the spatial SST patterns across the North Atlantic, observed under
293   global warming, are significantly suppressed under SAI (Figs. 3f and 4f). This response of AMO to SAI
294   is compatible with the observed changes in AMO imposed by anthropogenic and volcanic aerosols
295   reported by Masson-Delmotte et al. (2021). Anthropogenic and volcanic aerosols are understood to
296   have impacted the timing and magnitude of the cold (negative) episode in the historical AMO record
297   between the mid-1960s and mid-1990s and succeeding warming (Masson-Delmotte et al., 2021).
298   Anthropogenic aerosols have also been suspected as impacting historical SSTs elsewhere,
299   particularly the decadal ENSO variability (e.g., Sutton and Hodson, 2007; Westervelt et al., 2018).
300
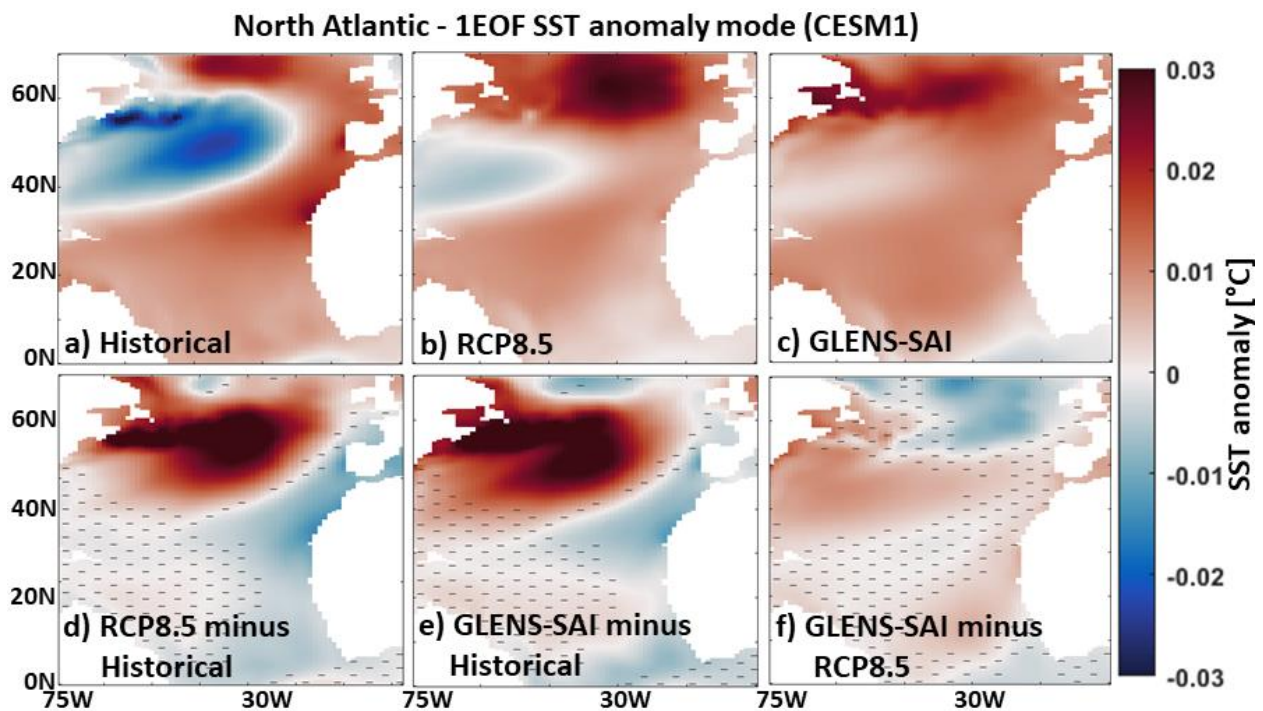
302   **Figure 3.** The first EOF (1EOF) patterns of SST anomaly across the North Atlantic relate to the AMO
303   index simulated by CESM1 for the historical data (a) and the mean of the available ensemble
304   members outputs under the RCP8.5 (b) and GLENS-SAI (c) scenarios. The maps at the bottom row
305   show RCP8.5 minus historical (d), GLENS-SAI minus historical (e), and GLENS-SAI minus RCP8.5 (f)
306   where the hatched patterns are not statistically significant (p>0.05), based on p-values from t-test
307   analysis.
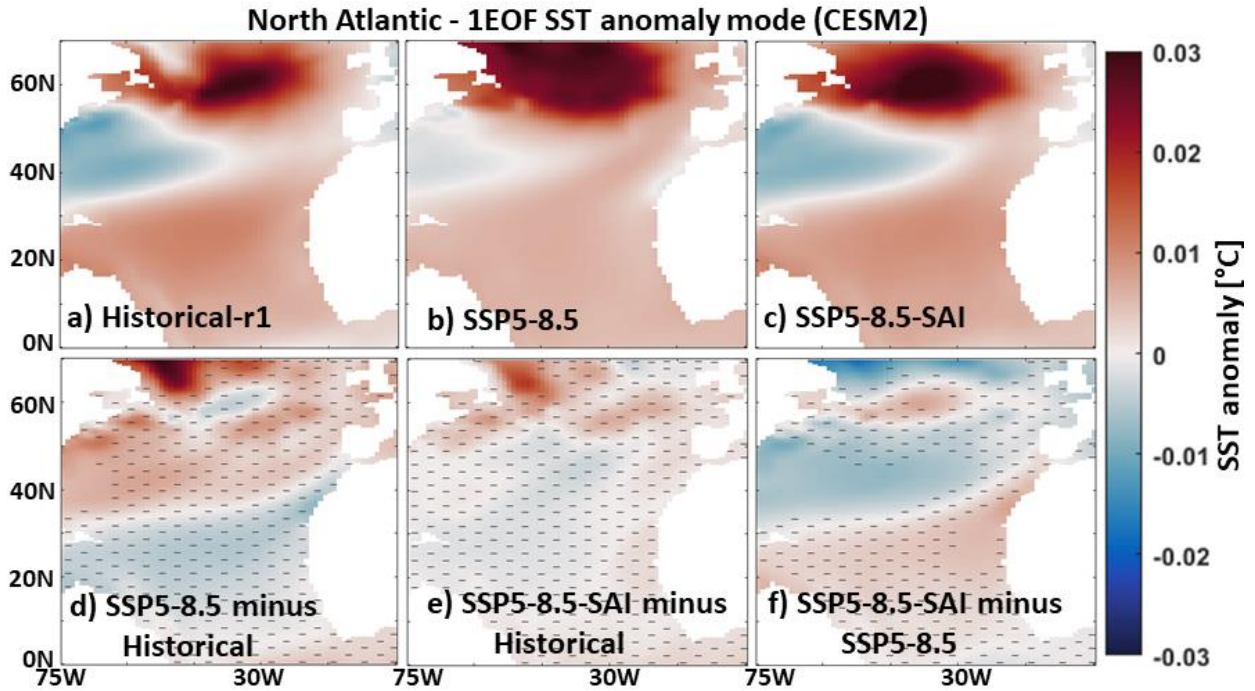
Figure 4. As in Fig. 3, but for CESM2 and SSP5-8.5.

The leading EOF of monthly global SST anomalies corresponding to the ENSO mode (Figs. S2 and S3), and is seen as a warm-tongue pattern over the tropical Pacific, that exhibits very similar patterns under both global warming and SAI scenarios as in the historical period. However, Fig. S4 shows that the warm-tongue pattern in CESM1 and CESM2 has an excessive westward extension relative to observations, which is compatible with the findings of Capotondi et al. (2020).

While the first EOF SST anomaly across the North Pacific under both global warming and SAI scenarios in CESM1 and CESM2 (Figs. 5 and 6) exhibits a similar cold-tongue pattern (typical of the North Pacific) as in the historical period. A lower contrast between the cold-tongue pattern and its surroundings is observed under SSP5-8.5 (Fig. 6b), which is effectively compensated by the geoengineering scenarios of SSP5-8.5-SAI through a significant SST decrease over middle North Pacific (Fig. 6c and 6f) since there is no significant change between SAI and historical maps (Fig. 6e). There is an excessive eastward expansion of the cold-tongue pattern with cooler temperatures under the SAI scenario as simulated by the CESM1 (Fig. 5c), which is due to the significant cooling of the water in the outside of the cold-tongue pattern imposed by the SO_2 injection (Fig. 5e-f).
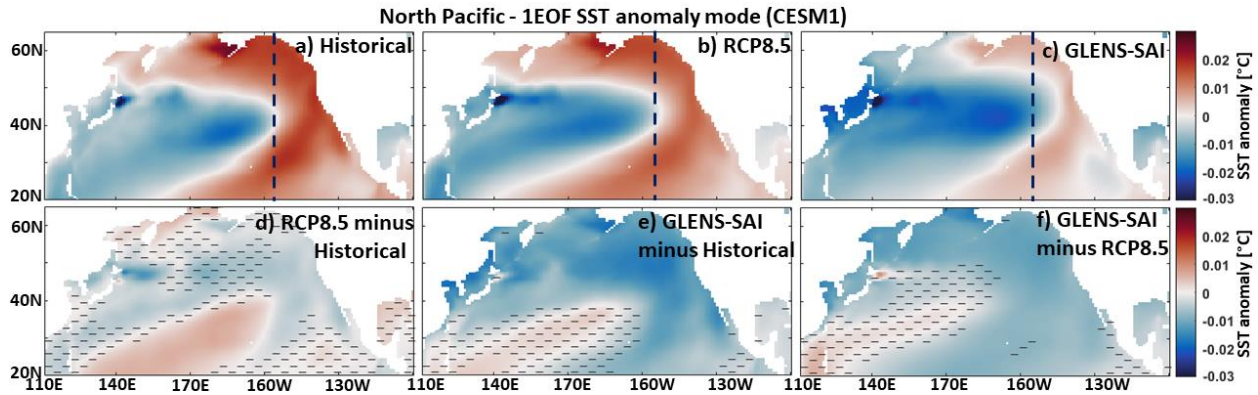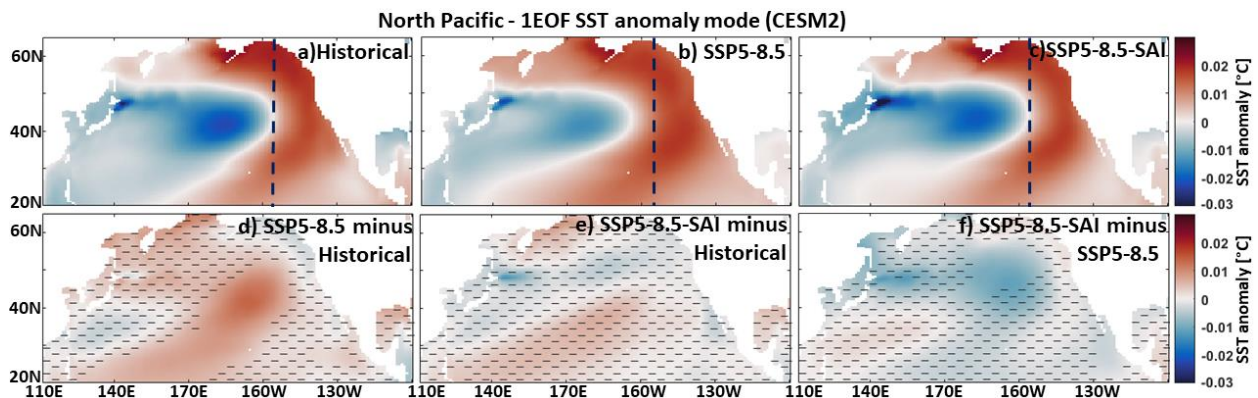
Figure 5. As Fig. 3 but across the North Pacific relates to the PDO index.


Figure 6. As in Fig. 5, but for CESM2.

3.2. Temporal evolution of indices

Figure 7 displays the projected changes in the El Niño and La Niña episodes in the ENSO index under global warming and SAI. The global warming scenario simulated by CEMS2 tends to reduce the time between, as well as the intensity and duration of the La Niña episodes compared to the historical conditions, but El Niño shows no significant changes. Frequency increases in both El Niño and La Niña episodes were suggested in earlier climate simulations e.g., Fredriksen et al. (2020), Cai et al. (2014) and Yun et al. (2021) for El Niño, and Cai et al. (2015) for La Niña. In contrast, using CESM1, the characteristic changes of El Niño are stronger than that of La Niño and the El Niño intensity significantly increases while its duration decreases relative to historical period. The La Niña intensity significantly increases but other characteristics show no significant changes under RCP8.5.

For CESM2, although the SAI is mostly accompanied by a slight decrease in the median of El Niño/La Niña characteristics towards their historical value, its effect on global warming imposed-changes is only statistically significant for the intensity and duration of La Niña events. For the CESM2 SAI

14

346 experiment, there are no significant differences in El Niño characteristics as with the GHG forcing
347 experiment. In contrast La Niña peak intervals, height (i.e., intensity), and width (i.e., duration)
348 characteristics are significantly different from GHG forcing and reverse the direction of changes
349 imposed by GHG. For CESM1, there are no significant differences between the results from RCP8.5
350 and GLENS-SAI scenarios.

351
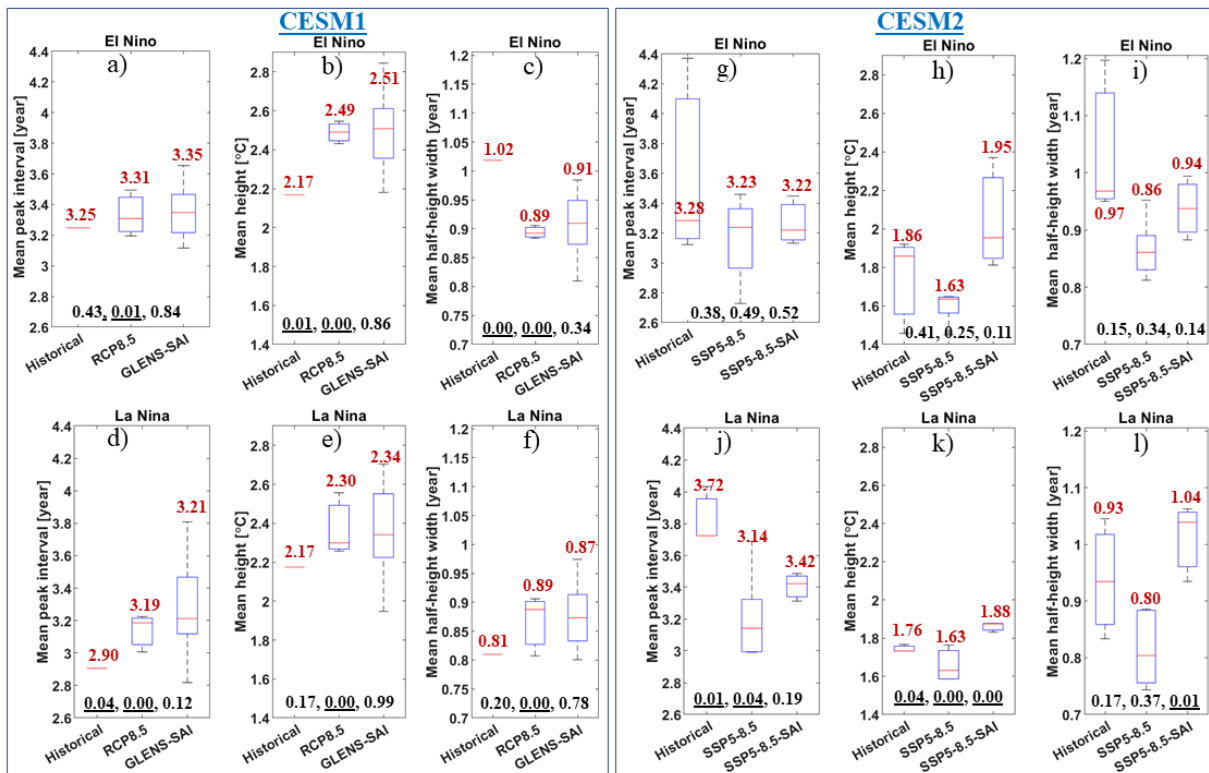
Figure 7. The projected changes in the mean peak interval, height, and half-height width of El Niño and La Niña events for global warming (RCP8.5 and SSP5-8.5) and SAI (GLENS-SAI and SSP5-8.5-SAI) scenarios simulated by CESM1 (panels a-f) and CESM2 (panel g-l). The median for each experiment is denoted by the red line, the upper (75th) and lower (25th) quartiles by the top and bottom of the box and ensemble limits by the whisker extents. The values labeled in red on each box show their median. The three values shown at bottom of each sub-plot refer to the p-values obtained from the statistical t-test between historical and global warming, historical and SAI, and global warming and SAI, respectively. Values underlined are significant (i.e., p<0.05).

362 Another way to illustrate the temporal evolution of signals is by using the power spectrum. Figures
363 8 and S5 compare the changes in temporal variability of each climate indices (AMO, NAO, ENSO, and
364 PDO) using the global power spectrums of CWTs under the global warming and SAI scenarios
365 simulated by CESM2, excluding CESM1 outputs as there is just a single ensemble member for CESM1
366 historical data over a short 1980-2009 period. In CESM1, the signals longer than 25 years, which are
367 the most energetic modes in observations of the PDO (Mantua and Hare, 2002) and AMO (Enfield et

368 al., 2001), cannot be captured in the historical simulations owing to their short simulation period

369 (1980-2009). As an example, Fig. S5 shows the ENSO CWTs and their global power spectrums for

370 historical, SSP5-8.5, and SSP5-8.5-SAI scenarios.

371 The inter-annual modes of AMO, NAO, and ENSO are preserved under both global warming and SAI.

372 For the decadal and longer periodicities, SAI accentuates AMO changes induced by GHG (Fig. 8a). For

373 example, the dominant modes at 20-30- and 55-85-year of the AMO, observed during the historical

374 period, show no significant changes under global warming; however, they vanish under SAI. The

375 decadal 10-20-years mode of the historical NAO is not preserved in the global warming scenario nor

376 with SAI (Fig. 8b). For ENSO, the dominant historical inter-annual modes show no significant change

377 under both global warming and SAI, except that its power under SAI is stronger (Fig. 8c). The

378 dominant modes at 10-20- and 50-70-years, observed in historical PDO (consistent with the real

379 PDO's dominant modes (Mantua et al., 1997)), are not present in both the SSP5-8.5 and SAI

380 simulations, and the latter two are similar to each other (Fig. 8d). In contrast with the historical

381 period in which the dominant modes of PDO occur in the 10-20- and 50-70-year bands, the dominant

382 modes under global warming (i.e., SSP5-8.5) and SAI (i.e., SSP5-8.5-SAI) occur at the ~10-year period.

383 The PDO shift to a higher frequency with decadal/multi-decadal variability weakness, observed

384 under global warming, was also earlier demonstrated by Fang et al. (2014) with a previous

385 generation of the climate model, the Fast Ocean Atmosphere Model (FOAM) used in IPCC AR4

386 experiments. Likewise, the PDO timescale has been simulated to decrease from ~20 to ~12 years

387 under global warming (Fedorov et al., 2020), possibly because of changes in the phase speed of

388 internal Rossby waves and ocean stratification (Zhang and Delworth, 2016). Nonetheless, although

389 PDO cycles between 30-50-year bands show slightly stronger power under SAI than global warming,

390 the 30-50-year is not the dominant PDO mode under SAI in contrast to Zhang and Delworth's (2016)

391 results for cooler climates, which the PDO dominant variability shifts to lower frequency (~34 yr).

392 They related this increase to weaker ocean stratifications accompanied by global cooling. However,

393 Zhang and Delworth (2016) used a different model (Geophysical Fluid Dynamics Laboratory coupled

394 model version 2.5 through the forecast-oriented low ocean resolution version) and experiments

395 ($2\times CO_2$ for global warming and $0.5\times CO_2$ for cooling).

396 We further analyzed the concatenated series from the available members for each scenario using

397 CESM2 to statistically capture the low frequency cycles with better reliability. Figure S6 summarizes

398 the CWT global power spectrums for AMO, NAO, ENSO, and PDO. The results, on the whole, are

399 compatible with those shown in Fig. 8, despite small discrepancies such as the much stronger

400 interdecadal mode in AMO obtained from the concatenated ensembles.
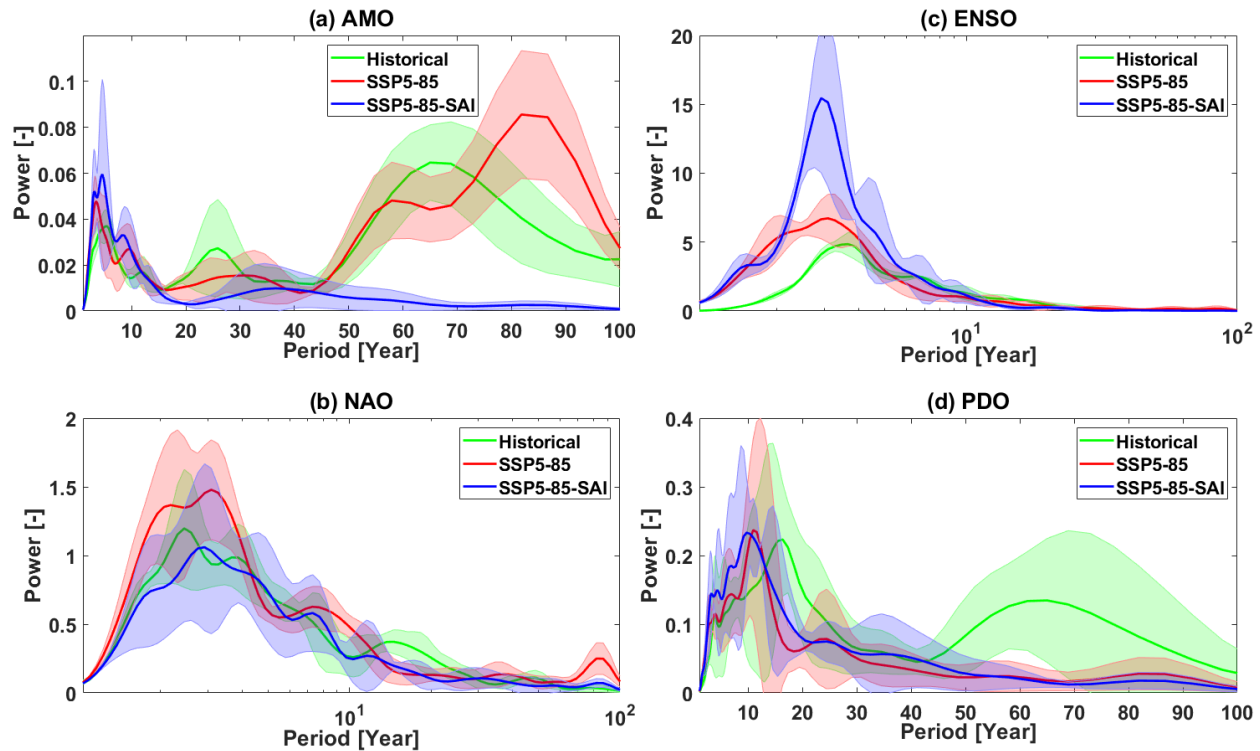
Figure 8. The CWT global power spectrums obtained for the indices of AMO (a), NAO (b), ENSO (c), and PDO (d) under SSP5-8.5 and SSP5-8.5-SAI relative to the historical results based on CESM2 for the periods of 1850-2014. Shading in each curve shows the across-ensemble range. The x-axis in NAO and ENSO graphs is on logarithmic scale.

4. Discussion

4.1. Caveats to interpretation

Caution is required when interpreting the results from this study with regard to real-world variability. Although CESM2 is highly rated among existing climate models, large model–observation differences are nonetheless present (Fasullo, 2020). Model-observation differences are larger in the earlier CESM1 version than in CESM2. For example, CESM1 exhibited a Subtropical (Azores) high anomaly (related to NAO) that was too weak but its representation is improved in CESM2 (Simpson et al., 2020). We also find large differences in amplitude and variance of climate indices simulated by both CESM1 and CESM2 relative to the observations over the 1980-2009 period. The amplitude of the dominant EOF of the ENSO-related SST-anomaly modeled in both CESM1 and CESM2 is about twice the observations for the historical (1980-2009) period (Figs. S4 and S7). Figure S7 further shows NAO and PDO dominant mode amplitudes are lower in the model projections than in observations over the historical period. Additionally, the ENSO-associated SST anomaly pattern in the tropical Pacific shows an excessive westward extension under both CESM1 and CESM2 (Fig. S4).

17

421 These limitations mirror those by Capotondi et al. (2020) for CESM2 in simulating the ENSO, who
422 suggested further work to illuminate how the physical parameterizations impact the key ENSO
423 feedback. Additionally, although CESM2 simulates the pattern of the summer and winter NAO well
424 over the historical period 1979-2014, the large uncertainties in specific members and in the historical
425 observations mean it is difficult to be quantitative about this (Simpson et al., 2020). However, CESM1
426 tends to underestimate the observed SST fluctuations in the Atlantic, leading to an underestimation
427 of the forced response (Undorf et al., 2018).

428 CMIP models tend to systematically underestimate the low-frequency signals (i.e., PDO) in the North
429 Pacific (Fasullo et al., 2020), owing in part to an imperfect modeling of decadal-scale structures in
430 these simulations (Masson-Delmotte et al., 2021). Compared to observational estimates, the decadal
431 variability in the subpolar North Atlantic SST appears to be slightly intensified through CMIP6
432 (Masson-Delmotte et al., 2021). How well we, therefore, can potentially capture forthcoming changes
433 in climate indices' variability will be restricted by how good each model simulations are (Gabriel and
434 Robock, 2015).

435 The second limitation is disparities in the length of records (30 years for the historical period, roughly
436 90 years for GHG emissions, and 80 years for SAI scenarios) may hinder the direct comparison of
437 climate indices behavior between historical and future climate scenarios of global warming and SAI;
438 and thus, the number of El Niño/La Niña events as well as the significance of the longer periodicities
439 (i.e., decadal and inter-decadal) in power spectrums. Furthermore, these records explore variability
440 within the statistical assumptions of the methods, which may not be robust for non-stationary time
441 series where the Normality and independence assumptions inherent in the wavelet and t-tests would
442 not strictly hold. We are limited to the available simulations, and a 3-member ensemble for SAI under
443 CESM2 is inherently weaker than 20-member ensembles under CESM1. CESM1 has a shorter 30-year
444 historical period from 1980 to 2009 which could not capture the interdecadal variability modes of
445 the teleconnection patterns. Yet another limitation arises from the relatively low spatial resolution
446 of the models which may affect the spatial SST anomaly patterns. Furthermore, Holmes et al. (2019)
447 pointed out the models are too low resolution to resolve ocean eddies, which substantially contribute
448 to ENSO irregularity and predictability. The absence of the eddy process may also be associated with
449 bias in spatial patterns and other ENSO characteristics (Bellenger et al., 2014) in the CMIP models
450 (Cai et al., 2021). Global high-horizontal resolution climate models have been indicated to
451 significantly improve the ocean-atmosphere circulations such as ENSO (Masson et al., 2012). As an
452 example, Haarsma et al. (2016) pointed out that the High Resolution Model Intercomparison Project
453 for CMIP6 improves the understanding of the climate teleconnection patterns of large-scale

454 circulations such as ENSO, NAO, and PDO, which suggests that running these high-resolution models

455 with SAI scenario would be worthwhile.

456

457 **4.2. Implications for climate stability**

458 Teleconnection signals represent emergent properties of the non-linear climate system. The

459 behavior of the climate teleconnection patterns can be characterized via its oscillations. In its

460 simplest form, a stable pattern would represent a fixed point or a periodic oscillation, but with real

461 non-linear systems, a quasi-periodic oscillation over specific frequency bands is more likely (e.g., Ghil

462 et al., 2002). These quasi-periodic characteristic frequencies may change smoothly over time in a

463 linear system but may proceed towards chaotic solutions via frequency doubling in non-linear

464 systems. Moron et al. (1998) suggested that ENSO crossed a threshold in the early 1960s, and the

465 periodicity of the seasonally forced climatic oscillator increased abruptly. The notable decline in low-

466 frequency multi-decadal band components of the wavelet spectra of the indices we study,

467 accompanied by a concomitant increase in the variance of the decadal band is consistent with abrupt

468 frequency doubling. This can be expected in non-linear systems as the energy in the system is raised,

469 progressing along the pathway towards chaotic behavior and hence less predictability on decadal

470 timescales.

471 The impact of SAI on the energetics of the coupled system are to offset the GHG increases by design.

472 Hence, we might expect that SAI could therefore reduce or stop the progression towards chaotic

473 behavior. However, the real climate system is far more complex than a simple energy balance

474 calculation. SAI increases stratospheric heating (Visioni et al., 2020), and this leads to tropospheric

475 changes, especially in winds (Gertler et al., 2020), and tropical circulation (Cheng et al., 2022).

476 Furthermore, the large heat reservoir of the global ocean has been out of equilibrium with the

477 atmosphere for centuries of anthropogenic GHG emissions, and this excess heat cannot be dissipated

478 by SAI within the timeframe in the simulations. So, we may expect SAI to, at best, imperfectly reverse

479 the effects of GHG on teleconnections.

480 Ocean stratification (ocean buoyancy frequency) and the baroclinic Rossby wave in the North Pacific

481 play significant roles in SST amplitude and PDO cycles since enhanced ocean buoyancy frequency

482 speeds up the Rossby waves, and so the decadal and longer cycle weakening accompanies higher PDO

483 frequency (Fang et al., 2014). Ocean stratification changes predominantly in response to changes in

484 surface temperature and salinity (Fang et al., 2014). The North Atlantic and the northeast Pacific are

485 projected to be among those areas with the greatest stratification changes under global warming in

486 the second-half of the 21st century (Capotondi et al. 2012). Historical records also show that volcanic

487 sulfate aerosols have altered multi-decade SST variability in the North Atlantic and North Pacific

488 (Birkel et al., 2018).

489 While SAI effectively reverses the changes in the spatial patterns under GHG forcing across the North

490 Atlantic (i.e., AMO) and North Pacific (i.e., PDO) and compensates for modest changes in the

491 characteristics of the El Niño and La Niña episodes (related to the tropical Pacific), it does not

492 effectively suppress the projected changes in decadal (~10-20-year) and inter-decadal (longer than

493 ~20-year) variability of circulations imposed by global warming. Anthropogenic aerosols intensify

494 the inter-annual variability (particularly in ENSO) but weaken the longer than 10-year signals of the

495 ocean-atmosphere circulations, compatible with the multiyear to decadal variations in PDO (Hua et

496 al., 2018). SAI involves aerosols in the stratosphere not the troposphere, so the effects will be

497 different, not least because of stratospheric heating (Visioni et al., 2020). The cold-tong pattens in the

498 mid-latitude of both North Atlantic and North Pacific tend to have an excess eastward extension

499 under SAI, in line with the second-phase of the North Pacific response to large volcanic eruptions

500 (Wang et al., 2012), which are better analogues for SAI.

501 Whether the climate system in the model is representative of the earth can be diagnosed to some

502 extent by comparison of the historical simulation with observations. As noted in Section 4.1 both

503 CESM versions do present differences from observations, so they are not perfect. All climate models

504 are unavoidably uncertain (Knutti et al., 2002), mostly because of the imperfect understanding of

505 many of the interplays and feedbacks within the climate system (Jun et al., 2008). Previous analysis

506 of ENSO under SAI found no significant changes (Gabriel & Robock, 2015), but they used different

507 models with widely varying fidelity of modeled ENSO to observations, and much smaller simulated

508 quantities of SO_2 with the relatively modest RCP4.5 emissions scenario as a baseline. Furthermore,

509 in the only previous assessment of ENSO under SAI, by Gabriel and Robock (2015), SAI simulations

510 may not have been long enough to detect changes. The large 20-member ensemble of GLENS used in

511 this study may overcome this limitation, especially for short-period indices, since this represents

512 ~1600 model-years.

513 Changes in climate teleconnection patterns can indicate significant changes in the forcing. Such

514 changes are seen in time series analysis of teleconnection indices in the real world that coincide with

515 increased GHG (Tsonis et al., 2007; Wang et al., 2009). Wang et al (2009) note that regime shifts in

516 system behavior in the observations occurred when North Pacific and North Atlantic patterns

517 increase their coupling, and the key instigator is the NAO. The NAO's long-period counterpart, the

518 AMO, are seen in our simulations to change under SAI relative to GHG forcing at periods longer than

519 a decade. The historical NAO's decadal mode which vanished under global warming is not restored
520 by the simulated SAI.

521 The North Atlantic is an atypical region under SAI. The declines in heat transported northwards by
522 the AMOC under GHG forcing are, to great extent, reversed under all kinds of SRM including SAI (Xie
523 et al., 2022). Thus, great differences exist in SST and air/ocean heat flux between SAI and GHG
524 climates in the North Atlantic (Yue et al., 2021). If regime shifts occur when North Atlantic and Pacific
525 oceans increase their coupling, and if the decline in AMOC under GHG forcing decreases coupling
526 between the basins, then SAI may act to promote regime shift by reversing a decline in AMOC.

527 Many authors have noted that explosive volcanism, in some ways a natural analogue for SAI, is
528 accompanied by a positive episode of the NAO (e.g., Robock, 2000), and this may then be associated
529 with changes in multi-decadal AMO variability (Birkel et al., 2018). Furthermore, in the extreme
530 scenario of SAI being done such that temperatures are actually decreased then projected
531 strengthening of AMOC occurs (Tjiputra et al., 2016). However, it is also possible that regime shifts
532 induced by GHG forcing and the large temperature feedbacks they induce may dominate impacts over
533 those fairly subtle regime shifts in climate teleconnection patterns.

534

535 **5. Conclusions**

536 This study delivers a first overview of SAI response on the large-scale ocean-atmosphere circulations
537 of AMO, NAO, ENSO, and PDO using experiments based on CESM1(WACCM) and CESM2(WACCM6)
538 that apply stratospheric aerosol intervention through the injection of sulfur into the stratosphere,
539 GLENS-SAI and SSP5-8.5-SAI, respectively. The impacts of these interventions are assessed against
540 historical (1980-2009 for both the models and 1850-2014 for CESM2 in some analyses) and
541 projections under RCP8.5 and SSP5-85 (for the GLENS-SAI and SSP5-8.5-SAI, respectively). We found
542 that SAI effectively reverses the global warming-imposed changes in the variance of the leading EOF
543 SST anomaly associated with AMO, ENSO, and PDO. The SAI also effectively suppresses the changes
544 in the spatial patterns of the EOF SST anomaly across the North Atlantic (i.e., AMO) and North Pacific
545 (i.e., PDO). A decrease in the contrast between the cold-tongue pattern and its surroundings in the
546 North Pacific is further projected under GHG induced global warming, which the SAI successfully
547 restored.

548 CESM2 simulations suggest that increasing GHG emissions are accompanied by a modest increase in
549 the frequency of the El Niño and La Niña episodes but a modest decrease in their intensity and
550 duration. The SAI scenario effectively compensates for these changes.

551 In contrast to the impact of the SAI on the spatial patterns of the climate indices of AMO, PDO, and

552 ENSO, the SAI scenario does not effectively suppress the projected changes in decadal (~10-20-year)

553 and inter-decadal (longer than ~20-year) variability imposed by global warming. The decadal and

554 inter-decadal variability modes of all the historical climate indices (except for Atlantic-based indices

555 under SSP5-8.5) are not preserved in the GHG warming scenario and the SAI does not restore them.

556 Furthermore, compared to the historical 1850-2014 period in CESM2, SAI is projected to accentuate

557 AMO and have no effective impact on NAO at decadal and longer frequencies. Unlike the historical

558 period in which the long-period dominant modes of PDO occur in the 10-20- and 50-70-year bands,

559 the dominant modes under global warming are reduced to ~10-years, and the SAI does not restore

560 them.

561 The results exhibited here are particular to these types of future global warming scenarios and the

562 details of the SAI application, which deal with an extreme scenario of GHG emissions and continuous

563 increases in sulfur emissions. Furthermore, the findings are from ensemble members from just two

564 closely related models. Caution is warranted due to the model-observation differences, disparities in

565 the record length of the historical period compared to future climate scenarios, and the low spatial

566 resolution of the models. Nevertheless, our study does detect changes in climate teleconnection

567 signals, and hence underlying climate system dynamics under SAI when decomposed using EOF and

568 wavelet analyses.

569

574

575 **Competing interests:**

576 We confirm that there is no conflict of interest among the authors of this manuscript.

577

578 **Data availability:**

579 The data for CESM1 and CESM2 simulations are publicly available via their websites:

580 http://www.cesm.ucar.edu/projects/community-projects/GLENS/ (DOI: 10.5065/D6JH3JXX) and

581 https://esgf-node.llnl.gov/search/cmip6/.

582

583

584 **Author contribution:**

585 A. R.: Coordinated to analysis and the graphics of various figures and the manuscript preparation; Kh.

586 K. and S. T.: conceptualization and preparing the data; J. M. conceptualized and coordinated the

587 interpretation and discussion for various sections. All authors contributed to the discussion and

588 writing.

589

590 **References**:

591 Addison, P. S.: Introduction to redundancy rules: the continuous wavelet transform comes of

592   age, Philosophical Transactions of the Royal Society A: Mathematical, Physical and

593   Engineering Sciences, 376(2126), 20170258, https://doi.org/10.1098/rsta.2017.0258,

594   2018.

595 Abdelmoaty, H. M., Papalexiou, S. M., Rajulapati, C. R., and AghaKouchak, A.: Biases beyond the mean

596   in CMIP6 extreme precipitation: A global investigation, Earth's Future, 9(10),

597   e2021EF002196, https://doi.org/10.1029/2021EF002196, 2021.

598 An, S. I., and Wang, B.: Inter-decadal change of the structure of the ENSO mode and its impact on the

599   ENSO frequency, Journal of Climate, 13(12), 2044-2055, https://doi.org/10.1175/1520-

600   0442(2000)013<2044:ICOTSO>2.0.CO;2, 2000.

601 Bellenger, H., Guilyardi, É., Leloup, J., Lengaigne, M., and Vialard, J.: ENSO representation in climate

602   models: From CMIP3 to CMIP5, Climate Dynamics, 42(7), 1999-2018,

603   https://doi.org/10.1007/s00382-013-1783-z, 2014.

604 Birkel, S. D., Mayewski, P. A., Maasch, K. A., Kurbatov, A. V., and Lyon, B.: Evidence for a volcanic

605   underpinning of the Atlantic multidecadal oscillation, NPJ Climate and Atmospheric Science,

606   1(1), 1-7, https://doi.org/10.1038/s41612-018-0036-6, 2018.

607 Cai, W., Santoso, A., Collins, M., Dewitte, B., Karamperidou, C., Kug, J. S., ... and Zhong, W.: Changing El

608   Niño–Southern Oscillation in a warming climate. Nature Reviews Earth & Environment, 2(9),

609   628-644, https://doi.org/10.1038/s43017-021-00199-z, 2021.

610 Cai, W., Wang, G., Santoso, A., McPhaden, M. J., Wu, L., Jin, F. F., ... and Guilyardi, E.: Increased frequency

611   of extreme La Niña events under greenhouse warming, Nature Climate Change, 5(2), 132-

612   137, https://doi.org/10.1038/nclimate2492, 2015.

613 Cai, W., Borlace, S., Lengaigne, M., Van Rensch, P., Collins, M., Vecchi, G., ... and Jin, F. F.: Increasing

614   frequency of extreme El Niño events due to greenhouse warming, Nature climate

615   change, 4(2), 111-116, https://doi.org/10.1038/nclimate2100, 2014.

616 Capotondi, A., Deser, C., Phillips, A. S., Okumura, Y., & Larson, S. M.: ENSO and Pacific decadal
617   variability in the Community Earth System Model version 2, Journal of Advances in Modeling
618   Earth Systems, 12(12), e2019MS002022, https://doi.org/10.1029/2019MS002022, 2020.

619 Capotondi, A., & Sardeshmukh, P. D.: Is El Niño really changing?, Geophysical Research
620   Letters, 44(16), 8548-8556, https://doi.org/10.1002/2017GL074515, 2017.

621 Capotondi, A., Alexander, M. A., Bond, N. A., Curchitser, E. N., and Scott, J. D., Enhanced upper ocean
622   stratification with climate change in the CMIP3 models, Journal of Geophysical Research:
623   Oceans, 117(C4), https://doi.org/10.1029/2011JC007409, 2012.

624 Chen, X., and Tung, K. K.: Global-mean surface temperature variability: Space–time perspective from
625   rotated EOFs, Climate Dynamics, 51(5), 1719-1732, https://doi.org/10.1007/s00382-017-
626   3979-0, 2018.

627 Cheng, W., MacMartin, D. G., Kravitz, B., Visioni, D., Bednarz, E. M., Xu, Y., ... and Deng, X.: Changes in
628   Hadley circulation and intertropical convergence zone under strategic stratospheric aerosol
629   geoengineering, npj Climate and Atmospheric Science, 5(1), 32,
630   https://doi.org/10.1038/s41612-022-00254-6, 2022.

631 Cheng, L., Trenberth, K. E., Fasullo, J., Boyer, T., Abraham, J., and Zhu, J.: Improved estimates of ocean
632   heat content from 1960 to 2015, Science Advances, 3(3), e1601545,
633   https://doi.org/10.1126/sciadv.1601545, 2017.

634 Cook, B. I., Mankin, J. S., Marvel, K., Williams, A. P., Smerdon, J. E., and Anchukaitis, K. J.: Twenty-first
635   century drought projections in the CMIP6 forcing scenarios, Earth's Future, 8(6),
636   e2019EF001461, https://doi.org/10.1029/2019EF001461, 2020.

637 Dagon, K., and Schrag, D. P.: Exploring the effects of solar radiation management on water cycling in
638   a coupled land–atmosphere model. Journal of Climate, 29(7), 2635-2650,
639   https://doi.org/10.1175/JCLI-D-15-0472.1, 2016.

640 Danabasoglu, G., Lamarque, J. F., Bacmeister, J., Bailey, D. A., DuVivier, A. K., Edwards, J., ... and Strand,
641   W. G.: The community earth system model version 2 (CESM2), Journal of Advances in
642   Modeling Earth Systems, 12(2), e2019MS001916, https://doi.org/10.1029/2019MS001916,
643   2020.

644 Enfield, D. B., Mestas-Nuñez, A. M., and Trimble, P. J.: The Atlantic multidecadal oscillation and its
645   relation to rainfall and river flows in the continental US, Geophysical Research
646   Letters, 28(10), 2077-2080, https://doi.org/10.1029/2000GL012745, 2001.

647 Eyring, V., Bony, S., Meehl, G. A., Senior, C. A., Stevens, B., Stouffer, R. J., and Taylor, K. E.: Overview of
648   the Coupled Model Intercomparison Project Phase 6 (CMIP6) experimental design and

organization, Geoscientific Model Development, 9(5), 1937-1958, https://doi.org/10.1029/2000GL012745, 2016.

Fang, C., Wu, L., and Zhang, X.: The impact of global warming on the Pacific Decadal Oscillation and the possible mechanism, Advances in Atmospheric Sciences, 31(1), 118-130, https://doi.org/10.1007/s00376-013-2260-7, 2014.

Fasullo, J. T. and Richter, J. H.: Scenario and Model Dependence of Strategic Solar Climate Intervention in CESM, EGUsphere [preprint], https://doi.org/10.5194/egusphere-2022-779, 2022.

Fasullo, J. T., Phillips, A. S., and Deser, C.: Evaluation of leading modes of climate variability in the CMIP archives, Journal of Climate, 33(13), 5527-5545, https://doi.org/10.1175/JCLI-D-19-1024.1, 2020.

Fedorov, A. V., Hu, S., Wittenberg, A. T., Levine, A. F., and Deser, C.: ENSO Low-Frequency Modulation and Mean State Interactions, El Niño Southern Oscillation in a changing climate, 173-198, https://doi.org/10.1002/9781119548164.ch8, 2020.

Fedorov, A. V., and Philander, S. G.: A stability analysis of tropical ocean–atmosphere interactions: Bridging measurements and theory for El Niño, Journal of Climate, 14(14), 3086-3101, https://doi.org/10.1175/1520-0442(2001)014<3086:ASAOTO>2.0.CO;2, 2001.

Field, C. B., and Barros, V. R. (Eds.): Climate change 2014–Impacts, adaptation and vulnerability: Regional aspects, Cambridge University Press, 2014.

Fredriksen, H. B., Berner, J., Subramanian, A. C., and Capotondi, A.: How does El Niño–Southern Oscillation change under global warming—A first look at CMIP6, Geophysical Research Letters, 47(22), e2020GL090640, https://doi.org/10.1029/2020GL090640, 2020.

Gabriel, C. J., and Robock, A.: Stratospheric geoengineering impacts on El Niño/Southern Oscillation, Atmospheric Chemistry and Physics, 15(20), 11949-11966, https://doi.org/10.5194/acp-15-11949-2015, 2015.

Gertler, C. G., O'Gorman, P. A., Kravitz, B., Moore, J. C., Phipps, S. J., and Watanabe, S.: Weakening of the extratropical storm tracks in solar geoengineering scenarios, Geophysical Research Letters, 47(11), e2020GL087348, https://doi.org/10.1029/2020GL087348, 2020.

Ghil, M., Allen, M. R., Dettinger, M. D., Ide, K., Kondrashov, D., Mann, M. E., ... and Yiou, P.: Advanced spectral methods for climatic time series, Reviews of geophysics, 40(1), 3-1, https://doi.org/10.1029/2000RG000092, 2002.

Greene, C. A., Thirumalai, K., Kearney, K. A., Delgado, J. M., Schwanghart, W., Wolfenbarger, N. S., ... and Blankenship, D. D.: The climate data toolbox for MATLAB, Geochemistry, Geophysics, Geosystems, 20(7), 3774-3781, https://doi.org/10.1029/2019GC008392, 2019.

682 Grinsted, A., Moore, J.C., and Jevrejeva, S.: Application of the cross wavelet transform and wavelet
683   coherence to geophysical time series, Nonlinear Proc. Geoph. 11 (5-6), 561-566,
684   https://doi.org/10.5194/npg-11-561-2004, 2004.

685 Haarsma, R. J., Roberts, M. J., Vidale, P. L., Senior, C. A., Bellucci, A., Bao, Q., Chang, P., Corti, S., Fučkar,
686   N. S., Guemas, V., von Hardenberg, J., Hazeleger, W., Kodama, C., Koenigk, T., Leung, L. R., Lu,
687   J., Luo, J.-J., Mao, J., Mizielinski, M. S., Mizuta, R., Nobre, P., Satoh, M., Scoccimarro, E., Semmler,
688   T., Small, J., and von Storch, J.-S.: High Resolution Model Intercomparison Project
689   (HighResMIP v1.0) for CMIP6, Geosci. Model Dev., 9, 4185–4208,
690   https://doi.org/10.5194/gmd-9-4185-2016, 2016.

691 Holmes, R. M., McGregor, S., Santoso, A., and England, M. H.: Contribution of tropical instability waves
692   to ENSO irregularity, Climate Dynamics, 52(3), 1837-1855,
693   https://doi.org/10.1007/s00382-018-4217-0, 2019.

694 Hu, Z. Z., and Wu, Z.: The intensification and shift of the annual North Atlantic Oscillation in a global
695   warming scenario simulation, Tellus A: Dynamic Meteorology and Oceanography, 56(2), 112-
696   124, https://doi.org/10.3402/tellusa.v56i2.14403, 2004.

697 Hua, W., Dai, A., and Qin, M.: Contributions of internal variability and external forcing to the recent
698   Pacific decadal variations, Geophysical Research Letters, 45(14), 7084-7092,
699   https://doi.org/10.1029/2018GL079033, 2018.

700 Intergovernmental Panel on Climate Change (IPCC): Working Group I Contribution to the Sixth
701   Assessment Report (AR6), Climate Change 2021: The Physical Science Basis, 2021. Available
702   online: https://www.ipcc.ch/assessment-report/ar6/, 2007.

703 Joyce, T. M.: One hundred plus years of wintertime climate variability in the eastern United States, J.
704   Clim., 15, 1076–1086, https://doi.org/10.1175/1520-
705   0442(2002)015<1076:OHPYOW>2.0.CO;2, 2002.

706 Knutti, R., Stocker, T. F., Joos, F., and Plattner, G. K.: Constraints on radiative forcing and future climate
707   change from observations and climate model ensembles, Nature, 416(6882), 719-723,
708   https://doi.org/10.1038/416719a, 2002.

709 Jun, M., Knutti, R., and Nychka, D. W.: Spatial analysis to quantify numerical model bias and
710   dependence: how many climate models are there?, Journal of the American Statistical
711   Association, 103(483), 934-947, https://doi.org/10.1198/016214507000001265, 2008.

712 Kravitz, B., MacMartin, D. G., Mills, M. J., Richter, J. H., Tilmes, S., Lamarque, J. F., Tribbia, J. J. and Vitt,
713   F.: First simulations of designing stratospheric sulfate aerosol geoengineering to meet

714   multiple simultaneous climate objectives, Journal of Geophysical Research: Atmospheres,

715   122, 12,616–12,634, https://doi.org/10.1002/2017JD026874, 2017.

716 Kravitz, B., Caldeira, K., Boucher, O., Robock, A., Rasch, P. J., Alterskjaer, K., ... and Yoon, J. H.: Climate

717   model response from the geoengineering model intercomparison project (GeoMIP), Journal

718   of   Geophysical   Research: Atmospheres, 118(15),   8320-8332,

719   https://doi.org/10.1002/jgrd.50646, 2013.

720 Latif, M., and Keenlyside, N. S.: El Niño/Southern Oscillation response to global warming, Proceedings

721   of   the   National   Academy   of   Sciences, 106(49),   20578-20583,

722   https://doi.org/10.1073/pnas.0710860105, 2009.

723 Mantua, N., and Hare, S.: The Pacific Decadal oscillation, J. Oceanogr. 58 (1), 35–44.

724   http://dx.doi.org/10.1023/A:1015820616384, 2002.

725 Mantua, N. J., Hare, S. R., Zhang, Y., Wallace, J. M., and Francis, R. C.: A Pacific interdecadal climate

726   oscillation with impacts on salmon production, Bulletin of the american Meteorological

727   Society, 78(6),   1069-1080,   https://doi.org/10.1175/1520-

728   0477(1997)078<1069:APICOW>2.0.CO;2, 1997.

729 Masson-Delmotte, V., Zhai, P., Pirani, A., Connors, S. L., Péan, C., Berger, S., ... and Zhou, B.: Climate

730   change 2021: the physical science basis, Contribution of working group I to the sixth

731   assessment   report   of   the   intergovernmental   panel   on   climate   change, 2,

732   https://10.1017/9781009157896, 2021.

733 Masson, S., Terray, P., Madec, G., Luo, J. J., Yamagata, T., and Takahashi, K.: Impact of intra-daily SST

734   variability on ENSO characteristics in a coupled model, Climate dynamics, 39(3), 681-707,

735   https://doi.org/10.1007/s00382-011-1247-2, 2012.

736 Mills, M. J., Richter, J. H., Tilmes, S., Kravitz, B., MacMartin, D. G., Glanville, A. A., Tribbia, J. J., Lamarque,

737   J. F., Vitt, F., Schmidt, A. and Gettelman, A.: Radiative and chemical response to interactive

738   stratospheric sulfate aerosols in fully coupled CESM1(WACCM), Journal of Geophysical

739   Research: Atmospheres, 122, 13,061–13,078, https://doi.org/10.1002/2017JD027006,

740   2017.

741 Meinshausen, M., Lewis, J., McGlade, C., Gütschow, J., Nicholls, Z., Burdon, R., ... and Hackmann, B.:

742   Realization of Paris Agreement pledges may limit warming just below 2°

743   C, Nature, 604(7905), 304-309, https://doi.org/10.1038/s41586-022-04553-z, 2022.

744 Moore, J. C., Yue, C., Zhao, L., Guo, X., Watanabe, S., and Ji, D.: Greenland ice sheet response to

745   stratospheric aerosol injection geoengineering, Earth's Future, https://doi.org/10.1029/

746   2019EF001393, 2019.

Moore, J. C., Rinke, A., Yu, X., Ji, D., Cui, X., Li, Y., Alterskjaer, K., Kristjánsson, J. E., Muri, H., Boucher, O. and Huneeus, N.: Arctic sea ice and atmospheric circulation under the GeoMIP G1 scenario, Journal of Geophysical Research: Atmospheres, 119, 567–583, https://doi.org/10.1002/2013JD021060, 2014.

Moron, V., Vautard, R., and Ghil, M.: Trends, interdecadal and interannual oscillations in global sea-surface temperatures, Climate Dynamics, 14(7), 545-569, https://doi.org/10.1007/s003820050241, 1998.

Riahi, K., Rao, S., Krey, V., Cho, C., Chirkov, V., Fischer, G., ... and Rafaj, P.: RCP 8.5—A scenario of comparatively high greenhouse gas emissions, Climatic change, 109(1), 33-57, https://doi.org/10.1007/s10584-011-0149-y, 2011.

Robock, A.: Volcanic eruptions and climate, *Reviews of Geophysics*, 38(2), 191–219, https://doi.org/10.1029/1998RG000054, 2000.

Scafetta, N.: Testing the CMIP6 GCM Simulations versus surface temperature records from 1980–1990 to 2011–2021: High ECS is not supported, Climate, 9(11), 161, https://doi.org/10.3390/cli9110161, 2021.

Simpkins, G.: Breaking down the NAO–AO connection, Nature Reviews Earth & Environment, 2(2), 88-88, https://doi.org/10.1038/s43017-021-00139-x, 2021.

Simpson, I. R., Bacmeister, J., Neale, R. B., Hannay, C., Gettelman, A., Garcia, R. R., ... and Richter, J. H.: An evaluation of the large-scale atmospheric circulation and its variability in CESM2 and other CMIP models, Journal of Geophysical Research: Atmospheres, 125(13), e2020JD032835, https://doi.org/10.1029/2020JD032835, 2020.

Shukla, J.: Predictability in the midst of chaos: A scientific basis for climate forecasting, science, 282(5389), 728-731, https://doi.org/10.1126/science.282.5389.728, 1998.

Sutton, R. T., and Hodson, D. L.: Climate response to basin-scale warming and cooling of the North Atlantic Ocean, Journal of Climate, 20(5), 891–907, https://doi.org/10.1175/JCLI4038.1, 2007.

Tilmes, S., MacMartin, D. G., Lenaerts, J. T. M., van Kampenhout, L., Muntjewerf, L., Xia, L., Harrison, C. S., Krumhardt, K. M., Mills, M. J., Kravitz, B., and Robock, A.: Reaching 1.5 and 2.0 °C global surface temperature targets using stratospheric aerosol geoengineering, Earth Syst. Dynam., 11, 579–601, https://doi.org/10.5194/esd-11-579-2020, 2020.

Tilmes, S., Richter, J. H., Kravitz, B., MacMartin, D. G., Mills, M. J., Simpson, I. R., Glanville, A. S., Fasullo, J. T., Phillips, A. S., Lamarque, J. F. and Tribbia, J.: CESM1(WACCM) Stratospheric Aerosol

Geoengineering Large Ensemble Project, Bulletin of the American Meteorological Society, 99, 2361–2371. https://doi.org/10.1175/BAMSD-17-0267.1, 2018.

Tjiputra, J. F., Grini, A., and Lee, H.: Impact of idealized future stratospheric aerosol injection on the large-scale ocean and land carbon cycles, Journal of Geophysical Research: Biogeosciences, 121(1), 2-27, https://doi.org/10.1002/2015JG003045, 2016.

Trenberth, K. E.: The definition of El Niño, Bulletin of the American Meteorological Society, 78(12), 2771-2778, https://doi.org/10.1175/1520-0477(1997)078<2771:TDOENO>2.0.CO;2, 1997.

Tsonis, A. A., Swanson, K., and Kravtsov, S.: A new dynamical mechanism for major climate shifts, Geophysical Research Letters, 34(13), https://doi.org/10.1029/2007GL030288, 2007.

Undorf, S., Bollasina, M. A., Booth, B. B. B., and Hegerl, G. C.: Contrasting the effects of the 1850–1975 increase in sulphate aerosols from North America and Europe on the Atlantic in the CESM, Geophysical Research Letters, 45(21), 11-930, https://doi.org/10.1029/2018GL079970, 2018.

Visioni, D., MacMartin, D. G., Kravitz, B., Lee, W., Simpson, I. R., and Richter, J. H.: Reduced poleward transport due to stratospheric heating under stratospheric aerosols geoengineering, Geophysical Research Letters, 47(17), e2020GL089470, https://doi.org/10.1029/2020GL089470, 2020.

Wang, G., Swanson, K. L., and Tsonis, A. A.: The pacemaker of major climate shifts, Geophysical Research Letters, 36(7), https://doi.org/10.1029/2008GL036874, 2009.

Wang, C., and Dong, S.: Is the basin-wide warming in the North Atlantic Ocean related to atmospheric carbon dioxide and global warming?, Geophysical Research Letters, 37(8), https://doi.org/10.1029/2010GL042743, 2010.

Wang, T., Otterå, O. H., Gao, Y., and Wang, H.: The response of the North Pacific Decadal Variability to strong tropical volcanic eruptions, Climate Dynamics, 39, 2917-2936, https://doi.org/10.1007/s00382-012-1373-5, 2012.

Watson, A. J., Schuster, U., Bakker, D. C., Bates, N. R., Corbière, A., González-Dávila, M., ... and Wanninkhof, R.: Tracking the variable North Atlantic sink for atmospheric CO_2. Science, 326(5958), 1391-1393, https://doi.org/10.1126/science.1177394, 2009.

Westervelt, D. M., Conley, A. J., Fiore, A. M., Lamarque, J.-F., Shindell, D. T., Previdi, M., Mascioli, N. R., Faluvegi, G., Correa, G., and Horowitz, L. W.: Connecting regional aerosol emissions reductions to local and remote precipitation responses, Atmospheric Chemistry and Physics Discussions, 18, 12,461–12,475. https://doi.org/10.5194/acp-2018-516, 2018.

813 Xie, M., Moore, J. C., Zhao, L., Wolovick, M., and Muri, H.: Impacts of three types of solar geoengineering
814   on the Atlantic Meridional Overturning Circulation, Atmospheric Chemistry and
815   Physics, 22(7), 4581-4597, https://doi.org/10.5194/acp-22-4581-2022, 2022.

816 Yue, C., Schmidt, L. S., Zhao, L., Wolovick, M., and Moore, J. C.: Vatnajökull mass loss under solar
817   geoengineering due to the North Atlantic meridional overturning circulation, Earth's
818   Future, 9(9), e2021EF002052, https://doi.org/10.1029/2021EF002052, 2021.

819 Yun, K. S., Lee, J. Y., Timmermann, A., Stein, K., Stuecker, M. F., Fyfe, J. C., and Chung, E. S.: Increasing
820   ENSO–rainfall variability due to changes in future tropical temperature–rainfall
821   relationship, Communications Earth & Environment, 2(1), 1-7,
822   https://doi.org/10.1038/s43247-021-00108-8, 2021.

823 Zhang, L., and Delworth, T. L.: Simulated response of the Pacific decadal oscillation to climate
824   change, Journal of Climate, 29(16), 5999-6018, https://doi.org/10.1175/JCLI-D-15-0690.1,
825   2016.

826 Zhang, R., and Delworth, T. L.: Impact of Atlantic multidecadal oscillations on India/Sahel rainfall and
827   Atlantic hurricanes, Geophysical research letters, 33(17),
828   https://doi.org/10.1029/2006GL026267, 2006.